

Environment-Assisted Quantum Transport and Mobility Edges

Donny Dwiputra^{1,*} and Freddy P. Zen^{1,2,†}

¹*Theoretical Physics Laboratory, Faculty of Mathematics and Natural Sciences,
Institut Teknologi Bandung, Jl. Ganesha 10, Bandung 40132, Indonesia*

²*Indonesian Center for Theoretical and Mathematical Physics (ICTMP), Bandung 40132, Indonesia*
(Dated: November 18, 2021)

Environment-assisted quantum transport (ENAQT) is a unique situation where environmental noise can, counterintuitively, enhance the transport of an open quantum system. In this Letter, we investigate how the presence of a one-dimensional single-particle mobility edge can generate strong ENAQT. For this purpose, we study the energy current of a generalized Aubry-Andre-Harper (AAH) tight binding model coupled at its edges to spin baths of differing temperature and dephasing noise along the system. We find that the ENAQT increases by orders of magnitude and depends on the number of localized eigenstates and disorder strength nonmonotonically. We show that this enhancement is the result of the cooperative interplay between population spread and localization.

Introduction.—Understanding and controlling the out-of-equilibrium dynamics in open quantum systems are at the forefront of research in the field of quantum thermodynamics. One particular phenomenon which has attracted considerable attention, both theoretically [1–13] and experimentally [14–18], are the environment-assisted quantum transport (ENAQT) where moderate dephasing noise can enhance the transport efficiency. Fueled by the quest for sustainable energy, several studies have exploited the potential benefit from the interplay between coherence and dissipation in quantum devices such as to enhance the power of quantum heat engines [19–22]. Nonequilibrium disordered systems with localization properties can act as heat engine as work can be extracted from the transition between the athermal localized states to an equilibrium extended state [23]. Systems with mobility edge on the other hand may act as a current rectifier [24, 25] or an energy filter to obtain a strong thermoelectric response [26]. However, the link between ENAQT and mobility edge is far from clear.

ENAQT may be explained by different mechanisms: initially its origin is understood from the destruction of Anderson localization [27]—which hinders the transport—by dephasing in a disordered system [1–4, 6] such as the photosynthetic complex [28–31]. However, ENAQT persists in ordered systems, where localization does not play role, and in fact it is impossible *only* for transport in an ordered chain [7]. Thus it relies on a beneficial competition between coherent and incoherent dynamics which results in higher population entering the sink. In some specific cases, momentum rejuvenation [8], line-broadening [9], and superradiance [10] may additionally explain the high efficiency. Moreover, exposing the system to a periodic driving may increase the efficiency even further [12, 13]. It is only revealed recently that the uniformity of steady state population plays more universal role in ENAQT [11]. Consider a chain of qubit sites without static disorder: when the system is coupled only to a source and a sink (no environmental dephasing), be it a particle pulse or a current source, trans-

port is dominated by the unitary dynamics and thus the corresponding wave function spreads out with quantum interference pattern. Adding dephasing noise leads to decoherence in site basis, which in turn reduces the fluctuation and thereby uniformize the population. This increases the sink particle density and thus amplifying the current. In the limit of strong dephasing, transport is suppressed under the quantum Zeno effect [32]. For end-to-end transport, the population is already maximally spread; dephasing will only reduce the current unless localized eigenstates exist.

The interesting consequence of Anderson localization is the quantum phase transition between extended (metallic) and localized (insulating) states as a function of disorder strength. In one and two dimensions, all eigenstates are localized for a random (uncorrelated) disorder of any strength *independent* of energy while in three dimensions the localization transition occurs in a critical disorder strength forming a sharp mobility edge, i.e., a threshold energy value that separates localized and extended eigenstates. Yet if we replace the random disorder with a quasiperiodic potential such as the paradigmatic Aubry-Andre-Harper (AAH) model [33, 34], which has been realized in recent ultracold atom experiments with interacting and noninteracting particles [35–37], the localization transition occurs even in one dimension. Moreover, by introducing nonlocal hopping terms or deforming the on-site potential, the model can manifest an exact mobility edge [38–41], defined by the self-duality point.

In this Letter, we show that a thermodynamically model with single particle mobility edge (SPME) can manifest a strong ENAQT, measured by comparing the heat current to the one without dephasing. The population uniformization mechanism alone is not sufficient to explain the nonmonotonic behavior of ENAQT with the fraction of localized eigenstates; the spread of population does not always correlate with ENAQT. Instead, both population spread and localization must coexist in order to obtain the maximum enhancement. We also show that the maximum ENAQT varies nonmonotoni-

cally with disorder strength. To isolate the ENAQT from the enhancement due to interference effects, we consider an end-to-end transport.

Model.—We study a one-dimensional generalized AAH (GAAH) model [41] of N bosonic modes with nearest-neighbor hopping described by the Hamiltonian

$$H_S = -t \sum_{n=1}^{N-1} (a_n^\dagger a_{n+1} + \text{H.c.}) + \sum_{n=1}^N V_n a_n^\dagger a_n, \quad (1)$$

where $a_n (a_n^\dagger)$ is the usual bosonic annihilation (creation) operator at site n , t is the tunneling, which sets the energy unit. We consider zero and single-excitation manifolds given by the states $|0\rangle$ and $|n\rangle = a_n^\dagger |0\rangle$, so that the local modes $a_n = |0\rangle\langle n|$. The on-site potential is

$$V_n = \Delta + 2\lambda \frac{1 - \cos(2\pi\beta n + \phi)}{1 + \alpha \cos(2\pi\beta n + \phi)}. \quad (2)$$

Here λ sets the average disorder strength and the offset is chosen to be $\Delta = 2$ to avoid negative eigenvalues. We consider the mobility edge parameter $\alpha \in (-1, 1)$, which can be tuned to represent several limiting cases: $\alpha = -1$ corresponds to an ordered chain, $\alpha = 0$ is the original (scaled) AAH model, and $\alpha = 1$ contains singular potential. We set $\beta = (\sqrt{5} - 1)/2$ for a quasiperiodic modulation. This model has a SPME at $E_{\text{ME}} = 2\text{sgn}(\lambda)(|t| - |\lambda|)/\alpha + \Delta$. The phase ϕ does not vary the energy spectrum; it only shifts the position of the localized modes [41]. From hereafter, we set $\hbar = k_B = 1$ and $t = 1$ as the unit of energy.

The chain is coupled to two different environment: pair of thermal baths of noninteracting spins $\{\sigma_{\mu,l}\}$ at different temperatures to its edges, $l = \{1, N\}$; characterized by H_{SB_1} , and dephasing noise H_{SB_2} due to spin bath coupled to all the sites. The former generates energy (or heat) current and the latter creates fluctuation in site energies, which in turn destroy the coherence of the system. The total Hamiltonian is $H = H_S + \sum_{i=1}^2 (H_{B_i} + H_{SB_i})$, where $H_{B_1} = \sum_{l,\mu} \varepsilon_{\mu,l} \sigma_{\mu,l}^z$, $H_{B_2} = \sum_{m,\mu} \varepsilon_{\mu} \sigma_{\mu,m}^z$ with $n = \{1, \dots, N\}$, and the interactions

$$H_{SB_1} = \sum_{l,\mu} g_{\mu}^{(1)} (a_l + a_l^\dagger) (\sigma_{\mu,l}^+ + \sigma_{\mu,l}^-), \quad (3)$$

$$H_{SB_2} = \sum_{n,\mu} g_{\mu}^{(2)} a_n^\dagger a_n (\sigma_{\mu,n}^+ + \sigma_{\mu,n}^-), \quad (4)$$

where $\sigma_{\mu,n}^+ (\sigma_{\mu,n}^-)$ are the raising (lowering) operators for the μ -th spin coupled to site n . This treatment, which explicitly considers the dynamics of the current heat baths and the interactions, $H_{B_1} + H_{SB_1}$, guarantees a thermodynamically consistent model [42]. In contrast to the typical models where the particle is initiated in one site and transferred to an irreversible sink, here the particle enters and exits the heat baths at finite temperature.

To derive the Lindblad master equation [43–47] for the density matrix ρ , we work in the eigenbasis $|\eta_k\rangle =$

$\sum_n S_{nk} |l\rangle$. In this basis, the system Hamiltonian becomes $H_S = \sum_k \epsilon_k \eta_k^\dagger \eta_k$ and the local mode is $a_n = \sum_k S_{nk} \eta_k$, where ϵ_k is the k -th energy (arranged in increasing order) and η_k and η_k^\dagger being its eigenmode operators. The corresponding master equation is

$$\begin{aligned} \frac{d\rho}{dt} = & -i[H, \rho] \\ & + \sum_{l,k} |S_{lk}|^2 J(|\epsilon_k|) [(1 - n_l(\epsilon_k)) \mathcal{D}[\eta_k] \rho + n_l(\epsilon_k) \mathcal{D}[\eta_k^\dagger] \rho] \\ & + \sum_{n,k < k'} |S_{nk}|^2 |S_{nk'}|^2 \gamma(|\epsilon_{k'} - \epsilon_k|) \mathcal{D}[\eta_k^\dagger \eta_{k'}] \rho, \end{aligned} \quad (5)$$

where the dissipator is $\mathcal{D}[A]\rho = A\rho A^\dagger - 1/2\{A^\dagger A, \rho\}$ and $n_l(\epsilon_k) = (e^{\epsilon_k/T_l} + 1)^{-1}$ is the spin occupation of the bath coupled to the edge site l . These superoperators describe a nonequilibrium condition in which energy is constantly pumped and absorbed at both ends, while dephasing occurs at every eigenmodes. $J(\epsilon)$ and $\gamma(\epsilon)$ are the spectral density of system-bath interaction H_{SB_1} and H_{SB_2} , respectively. Here we have assumed that B_2 is at $T = 0$ so that its occupation factor $n(\epsilon) \rightarrow 0$; this results in condition $\epsilon_k < \epsilon_{k'}$ and thus the sum is for $k < k'$. Since we have no information about the system-bath coupling, we assume for simplicity that $J(\epsilon_k) = 1$ and $\gamma(|\epsilon_{k'} - \epsilon_k|) = \gamma$ for all k and k' . Nevertheless, Ohmic spectral density $J(\epsilon) \propto \epsilon$ will produce similar results.

The nonequilibrium steady-state (NESS) can be calculated exactly once the Hamiltonian is diagonalized. The density matrix can be solved iteratively from $k = N$:

$$\langle \eta_k^\dagger \eta_k \rangle = A_k^{-1} \left(B_k + \gamma \sum_{i>k}^N C_{ik} \langle \eta_i^\dagger \eta_i \rangle \right), \quad (6)$$

with the coefficients

$$\begin{aligned} A_k &= \sum_l |S_{lk}|^2 (1 - 2n_l(\epsilon_k)) + \gamma \sum_{i<k} C_{ik}, \\ B_k &= \sum_l |S_{lk}|^2 n_l(\epsilon_k), \quad C_{ik} = \sum_n |S_{ni}|^2 |S_{nk}|^2, \end{aligned} \quad (7)$$

while the off-diagonal components are zero. Note that this state needs to be normalized. The peculiar factor 2 in A_k appears because the system and the bath have different statistics. The dephasing part of Eq. (5) transfers the population from the higher energy eigenmode $|\eta_{k'}\rangle$ to the lower energy $|\eta_k\rangle$ (since $k < k'$). This can be inferred from the last term in Eq. (6) in which C_{ik} measures the coupling between two eigenmodes in presence of dephasing. To determine ENAQT we consider the NESS energy current \mathcal{J} [48],

$$\begin{aligned} \mathcal{J} &= -\text{Tr}[H \mathcal{D}_N \rho] \\ &= \sum_k \epsilon_k |S_{Nk}|^2 \left((1 - 2n_N(\epsilon_k)) \langle \eta_k^\dagger \eta_k \rangle - n_N(\epsilon_k) \right), \end{aligned} \quad (8)$$

where \mathcal{D}_N is the sum of SB_1 superoperators acting on site N .

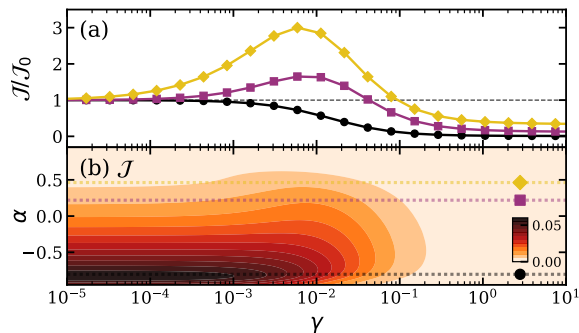


FIG. 1. (a) Relative current J/J_0 versus the dephasing rate γ for different mobility edge parameters α . Each solid line corresponds to horizontal lines crossing the (α, γ) contour plot of unnormalized current J with the same colors and symbols in (b). The parameters are $\lambda = 0.4$, $\phi = \pi/3$, and the bath temperatures $T_h = 10^3$ (at $l = 1$) and $T_c = 10^{-1}$ (at $l = N$). ENAQT occurs when $J/J_0 > 1$ in (a) or when a line segment in (b) crosses increasing contour.

Results.—To capture both ENAQT and mobility edge features, we choose a relatively short chain of $N = 22$ so that dephasing does not completely suppress the current, but still large enough to pronounce the mobility edge. The ENAQT, defined by J/J_0 , is measured by comparing a current J relative to the one without dephasing, $J_0 \equiv J(\gamma = 0)$; ENAQT is achieved when $J/J_0 > 1$.

In Fig. 1(a) we report the relative current J/J_0 with γ for different α 's corresponding to each dotted line in Fig. 1(b). We observe that between $\alpha = -1$ (uniform chain) and $\alpha = 0$, J/J_0 is almost always decreasing monotonically, indicating little to no ENAQT. This behavior is expected because for an end-to-end transport, ENAQT does not exist unless static disorder is introduced. For negative α , even though all eigenstates are delocalized, the weak disorder may still reduce the spread of site population. This allows a moderate dephasing to spread the population more evenly, producing small ENAQT. For $\alpha > 0$, the ENAQT is more pronounced through non-monotonic J/J_0 . Moreover, as α is closer to 0.5, the range of γ 's for which the ENAQT appears increases significantly.

The parameter region in which ENAQT exists is illustrated more clearly in Fig. 2(a). If we consider the spread of the NESS population to be the universal mechanism [11] underlying the ENAQT—higher spread yields higher current—then the highest relative current should be at the highest α , since higher α gives more localized eigenstates and thus allowing the dephasing to do more spreading (note that the spread of population in eigenbasis is same as in the site basis as we will define the spread with basis independent quantity). However, it turns out that the highest relative current is achieved not at the highest α but at $\alpha \approx 0.6$. This indicates that the spreading mechanism is not the whole story. Instead, the strength of

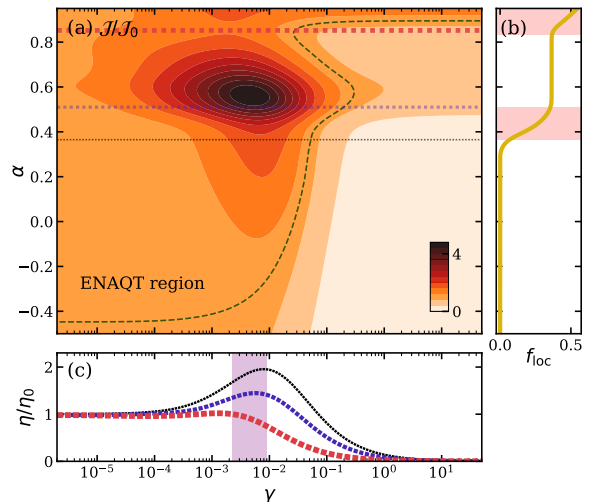


FIG. 2. (a) Contour plot of relative current J/J_0 as a function of α and γ . The dashed line corresponds to $J/J_0 = 1$ and thus separates the regions with and without ENAQT. (b) Fraction of localized eigenstates f_{loc} for each α . The shaded areas highlight the transition points at which f_{loc} varies significantly. (c) Relative spread η/η_0 as a function of γ . Each line is for different value of α which corresponds to horizontal lines in (a) with same color for each and increasing thickness for increasing α . The shaded area in (c) highlight the peaks of η/η_0 . The maximum for each α lines in (a) also occurs at similar location with the maximum of η/η_0 . The parameters are the same as in Fig. 1.

ENAQT must rely on the interplay between spreading and mobility edge.

To understand the role of the mobility edge, we study the relative current together with localization properties of the GAAH model. This is simply revealed by the fraction of localized eigenstates f_{loc} . A state is localized if its energy is, for $\alpha > (<)$ 0, larger (lower) than the SPME energy E_{ME} . By comparing Fig. 2(a) and (b), we observe that the contour width of ENAQT region varies quite significantly at the transition points of f_{loc} , that is highlighted by the shaded area around $\alpha \approx 0.4$ and $\alpha \approx 0.9$. To study the interplay between spreading and mobility edge, here we also calculate the population spread for several α 's, which we quantify using the normalized von Neumann entropy, $\eta = -\sum_k p_k \log p_k / \log N$, where $p_k = \langle \eta_k^\dagger \eta_k \rangle$ is given by Eq. (6). $\eta = 0$ is when a single eigenvalue dominates the population and $\eta = 1$ corresponds to uniform population. This measure has the advantage of being basis independent. In Fig. 2(c) we compare the relative spread, η/η_0 with $\eta_0 \equiv \eta(\gamma = 0)$, for α corresponding to transition points of f_{loc} in Fig. 2(b). Note that the maximum ENAQT, the peak of J/J_0 , and the maximum η/η_0 have different locations. The former is at $\alpha \approx 0.6$ and the latter is at $\alpha \approx 0.3$; both occur at similar $\gamma \lesssim 10^{-2}$. Thus higher relative spread does not guarantee higher ENAQT, since for higher α

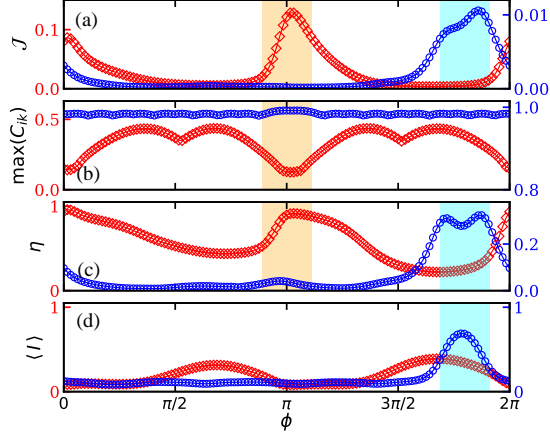


FIG. 3. For $\alpha = 0.1, \gamma = 0.006$ (red \diamond ; left y axis) and $\alpha = 0.9, \gamma = 1$ (blue \circ ; right y axis): (a) current \mathcal{J} versus phase ϕ , (b) maximum of coupling between two eigenmodes in presence of dephasing C_{ik} , (c) spread η as a function of ϕ , and (d) average inverse participation ratio $\langle I \rangle$. All plots are for the common disorder strength $\lambda = 0.4$. Shaded areas highlight the correlations between the quantities (see text).

the NESS is more localized, and consequently the dephasing can carry out more spreading which results in higher ENAQT. However, for $0.6 < \alpha < 0.8$ (the f_{loc} plateau), despite the stable f_{loc} , the relative spread is decreasing and thus also for the relative current. In the plateau regime, the relative spread fully controls the fate of ENAQT; it keeps decreasing until increases again due to the second f_{loc} transition around $\alpha = 0.9$. Moreover, η/η_0 also captures the f_{loc} transition and thus it is sensitive to mobility edges at low γ 's (see Supplemental Material [47]). Hence, we find that the cooperative interplay between population spread and localization determines the fate of ENAQT.

The feature of ENAQT in this model can be explored further by varying the phase ϕ . This can be achieved in experiments typically by shifting the phase of bichromatic laser field. The phase does not vary the number of localized states, Nf_{loc} , but it alters the spectrum S_{nk} . Consequently, the position of the localized states and the coupling between two modes C_{ik} in Eq. (7) are changed, resulting a substantial change in ENAQT and localization strength. To study the sensitivity of localization to the dephasing we calculate the average inverse participation ratio (IPR) $\langle I \rangle = \sum I_k p_k$ where $I_k = \sum_n |S_{nk}|^4$ is the IPR for the individual eigenstates.

Figure 3(a) shows \mathcal{J} as a function of ϕ for two cases: $\alpha = 0.1, \gamma = 6 \times 10^{-3}$ as the example for maximum ENAQT in the delocalized α regime (red \diamond ; $f_{\text{loc}} = 0$), and $\alpha = 0.9, \gamma = 1$ (blue \circ ; $f_{\text{loc}} \approx 0.5$) for the localized regime. Both currents have peaks in different ϕ 's and are suppressed in overlapping range. For instance, both currents are heavily suppressed around $\phi = \pi/2$ and $\phi = 3\pi/2$. Note that here we do not normalize \mathcal{J}

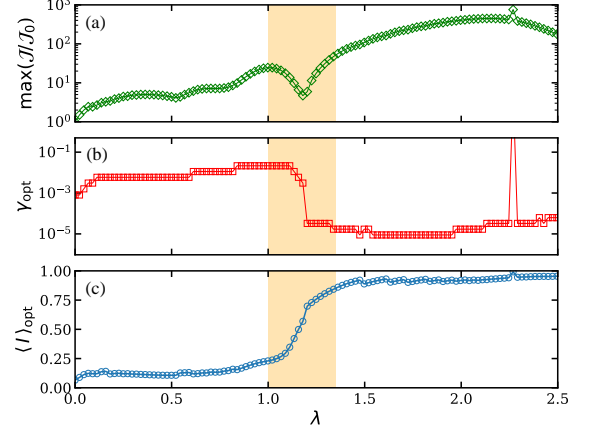


FIG. 4. (a) Maximum ENAQT, $\mathcal{J}/\mathcal{J}_0$, versus λ with $\phi = \pi/3$. (b) Dephasing rates at which maximum ENAQT in (a) occurs. (c) Average IPR for α_{opt} and γ_{opt} . Highlighted area indicates the values at localization transition.

for ENAQT as it is already for specific α and γ . For the delocalized regime, this can be explained solely by the maximum coupling between two eigenstates, $\max(C_{ik})$. The maximum value is always achieved for $i = k$ and thus it corresponds to $\max(C_{kk}) = \max_k(\sum_n |S_{nk}|^4)$, i.e., the maximum IPR I_k . We first turn our attention into the red \diamond line: in Fig. 3(b) we see that the \mathcal{J} is maximized whenever $\max(C_{ik})$ is small. The current is also maximized whenever the spread η is large (see Fig. 3(c)), confirming the previous result for low α regime that possesses ENAQT. We then proceed to the blue \circ line, where the f_{loc} is significantly higher than the previous one. Here the maximum coupling in Fig. 3(b) is no longer sensitive to ϕ , since there is always at least a localized state with IPR near unity for this case. On the other hand, the corresponding population spread and IPR in Fig. 3(c)–3(d) simultaneously determines the \mathcal{J} peak, in contrast to the previous (delocalized) case where \mathcal{J} relies solely on the population spread. Further analysis on the effect of α and ϕ to the spreading and localization in extended parameter can be found in the Supplemental Material [47].

To complete the phenomenology of this system, in Fig. 4(a) we plot the maximum ENAQT (achieved at certain α_{opt} and γ_{opt}) with disorder strength λ . It is possible to obtain $\mathcal{J}/\mathcal{J}_0 \approx 400$ for $\gamma \approx 10^{-5}$ (see Fig. 4(b)) at $\lambda \approx 2.1$. However, further increase in disorder strength reduces the maximum ENAQT as all eigenstates is maximally localized as indicated by $\langle I \rangle_{\text{opt}} \equiv \langle I \rangle(\alpha_{\text{opt}}, \gamma_{\text{opt}})$ near unity in Fig. 4(c) and the fact that all eigenstates are localized for $\lambda > 1$ and positive α . The localization transition in $\lambda = 1$ to $\lambda = 1.5$ is followed by a steep increase in the system sensitivity to dephasing by orders of magnitude, whereas giving a sharp transition for the maximum ENAQT due to the interplay between population spread and localization. In addition, small incre-

ments in Fig. 4(b) for $\lambda = 0$ to $\lambda = 1$ is followed by a series of local maxima in $\max(\mathcal{J}/\mathcal{J}_0)$. The fate of the maximum ENAQT along a γ_{opt} plateau is determined by α that gives the f_{loc} transition as in Fig. 2(a).

Conclusions.—We have studied how the presence of dephasing noise in a model with single particle mobility edge coupled to spin baths can manifest strong ENAQT. While the population spread alone may explain the origin of current enhancement, in localized regimes it cannot fully account for the nonmonotonic dependence of the mobility edge parameter and disorder strength. Instead, both the population spread and average IPR play a cooperative role where for highly localized eigenstates, the latter dominates the enhancement mechanism. Strong ENAQT thus maximizes at a specific mobility edge parameter near the f_{loc} transition and it can be tuned by shifting the position of the localized modes (by tuning the phase) and modifying the disorder strength.

It should be noted that the current is actually higher in the low α regime, below the mobility edge. However, if disorder or mobility edge are unavoidably present, or if in an engineered system the mobility edge is desired, the intermediate dephasing regime provides better performance. We briefly note that if particle interaction is included, the ENAQT features should similarly persist since the many-body localization occurs in the Hamiltonian [49, 50].

F.P.Z. thanks Ministry of Higher Education and Research of Indonesia for Research Funding P3MI ITB 2020. The numerical results were obtained using code written in NumPy [51] and QuTiP [52], and the figures were made using matplotlib [53].

* donny.dwiputra@s.itb.ac.id

† fpzen@fi.itb.ac.id

- [1] M. Mohseni, P. Rebentrost, S. Lloyd, and A. Aspuru-Guzik, Environment-assisted quantum walks in photosynthetic energy transfer, *J. Chem. Phys.* **129**, 11B603 (2008).
- [2] P. Rebentrost, M. Mohseni, I. Kassal, S. Lloyd, and A. Aspuru-Guzik, Environment-assisted quantum transport, *New J. Phys.* **11**, 033003 (2009).
- [3] P. Rebentrost, M. Mohseni, and A. Aspuru-Guzik, Role of quantum coherence and environmental fluctuations in chromophoric energy transport, *J. Phys. Chem. B* **113**, 9942 (2009).
- [4] M. B. Plenio and S. F. Huelga, Dephasing-assisted transport: quantum networks and biomolecules, *New J. Phys.* **10**, 113019 (2008).
- [5] A. Chin, S. Huelga, and M. B. Plenio, Coherence and decoherence in biological systems: principles of noise-assisted transport and the origin of long-lived coherences, *Philos. Trans. Royal Soc. A* **370**, 3638 (2012).
- [6] A. Chin, J. Prior, R. Rosenbach, F. Caycedo-Soler, S. F. Huelga, and M. B. Plenio, The role of non-equilibrium vibrational structures in electronic coherence and recoherence in pigment-protein complexes, *Nature Physics* **9**, 113 (2013).
- [7] I. Kassal and A. Aspuru-Guzik, Environment-assisted quantum transport in ordered systems, *New J. Phys.* **14**, 053041 (2012).
- [8] Y. Li, F. Caruso, E. Gauger, and S. C. Benjamin, ‘momentum rejuvenation’ underlies the phenomenon of noise-assisted quantum energy flow, *New Journal of Physics* **17**, 013057 (2015).
- [9] F. Caruso, A. W. Chin, A. Datta, S. F. Huelga, and M. B. Plenio, Highly efficient energy excitation transfer in light-harvesting complexes: The fundamental role of noise-assisted transport, *J. Chem. Phys.* **131**, 09B612 (2009).
- [10] G. P. Berman, A. I. Nesterov, G. V. López, and R. T. Sayre, Superradiance transition and nonphotochemical quenching in photosynthetic complexes, *J. Phys. Chem. C* **119**, 22289 (2015).
- [11] E. Zerah-Harush and Y. Dubi, Universal origin for environment-assisted quantum transport in exciton transfer networks, *J. Chem. Phys. Lett.* **9**, 1689 (2018).
- [12] D. Dwiputra, J. S. Kosasih, A. Sulaiman, and F. P. Zen, Driving-assisted open quantum transport in qubit networks, *Phys. Rev. A* **101**, 012113 (2020).
- [13] D. Dwiputra, A. Sulaiman, J. S. Kosasih, W. Hidayat, and F. P. Zen, Driving the dephasing assisted quantum transport, in *J. Phys. Conf. Ser.*, Vol. 1245 (IOP Publishing, 2019) p. 012075.
- [14] J. K. Sowa, J. A. Mol, G. A. D. Briggs, and E. M. Gauger, Environment-assisted quantum transport through single-molecule junctions, *Phys. Chem. Chem. Phys.* **19**, 29534 (2017).
- [15] D. N. Biggerstaff, R. Heilmann, A. A. Zecevik, M. Gräfe, M. A. Broome, A. Fedrizzi, S. Nolte, A. Szameit, A. G. White, and I. Kassal, Enhancing coherent transport in a photonic network using controllable decoherence, *Nat. Comm.* **7**, 11282 (2016).
- [16] N. Trautmann and P. Hauke, Trapped-ion quantum simulation of excitation transport: Disordered, noisy, and long-range connected quantum networks, *Phys. Rev. A* **97**, 023606 (2018).
- [17] H. Schempp, G. Günter, S. Wüster, M. Weidemüller, and S. Whitlock, Correlated exciton transport in rydberg-dressed-atom spin chains, *Phys. Rev. Lett.* **115**, 093002 (2015).
- [18] C. Maier, T. Brydges, P. Jurcevic, N. Trautmann, C. Hempel, B. P. Lanyon, P. Hauke, R. Blatt, and C. F. Roos, Environment-assisted quantum transport in a 10-qubit network, *Phys. Rev. Lett.* **122**, 050501 (2019).
- [19] K. E. Dorfman, D. V. Voronine, S. Mukamel, and M. O. Scully, Photosynthetic reaction center as a quantum heat engine, *Proc. Natl. Acad. Sci.* **110**, 2746 (2013).
- [20] M. O. Scully, K. R. Chapin, K. E. Dorfman, M. B. Kim, and A. Svidzinsky, Quantum heat engine power can be increased by noise-induced coherence, *Proc. Natl. Acad. Sci.* **108**, 15097 (2011).
- [21] F. Damanet, E. Mascarenhas, D. Pekker, and A. J. Daley, Controlling quantum transport via dissipation engineering, *Phys. Rev. Lett.* **123**, 180402 (2019).
- [22] A. Streltsov, G. Adesso, and M. B. Plenio, Colloquium: Quantum coherence as a resource, *Rev. Mod. Phys.* **89**, 041003 (2017).
- [23] N. Y. Halpern, C. D. White, S. Gopalakrishnan, and

- G. Refael, Quantum engine based on many-body localization, *Phys. Rev. B* **99**, 024203 (2019).
- [24] V. Balachandran, S. R. Clark, J. Goold, and D. Poletti, Energy current rectification and mobility edges, *Phys. Rev. Lett.* **123**, 020603 (2019).
- [25] M. Saha and S. K. Maiti, Particle current rectification in a quasi-periodic double-stranded ladder, *J. Phys. D Appl. Phys.* **52**, 465304 (2019).
- [26] C. Chiaracane, M. T. Mitchison, A. Purkayastha, G. Haack, and J. Goold, Quasiperiodic quantum heat engines with a mobility edge, *Phys. Rev. Res.* **2**, 013093 (2020).
- [27] P. W. Anderson, Absence of diffusion in certain random lattices, *Phys. Rev.* **109**, 1492 (1958).
- [28] G. S. Engel, T. R. Calhoun, E. L. Read, T.-K. Ahn, T. Mančal, Y.-C. Cheng, R. E. Blankenship, and G. R. Fleming, Evidence for wavelike energy transfer through quantum coherence in photosynthetic systems, *Nature* **446**, 782 (2007).
- [29] G. Panitchayangkoon, D. Hayes, K. A. Fransted, J. R. Caram, E. Harel, J. Wen, R. E. Blankenship, and G. S. Engel, Long-lived quantum coherence in photosynthetic complexes at physiological temperature, *Proc. Natl. Acad. Sci.* **107**, 12766 (2010).
- [30] H.-G. Duan, V. I. Prokhorenko, R. J. Cogdell, K. Ashraf, A. L. Stevens, M. Thorwart, and R. D. Miller, Nature does not rely on long-lived electronic quantum coherence for photosynthetic energy transfer, *Proc. Natl. Acad. Sci.* **114**, 8493 (2017).
- [31] S. J. Jang and B. Mennucci, Delocalized excitons in natural light-harvesting complexes, *Rev. Mod. Phys.* **90**, 035003 (2018).
- [32] B. Misra and E. G. Sudarshan, The zeno's paradox in quantum theory, *J. Math. Phys.* **18**, 756 (1977).
- [33] S. Aubry and G. André, Analyticity breaking and anderson localization in incommensurate lattices, *Ann. Israel Phys. Soc* **3**, 18 (1980).
- [34] P. G. Harper, Single band motion of conduction electrons in a uniform magnetic field, *Proc. Phys. Soc. London Sect. A* **68**, 874 (1955).
- [35] M. Schreiber, S. S. Hodgman, P. Bordia, H. P. Lüschen, M. H. Fischer, R. Vosk, E. Altman, U. Schneider, and I. Bloch, Observation of many-body localization of interacting fermions in a quasirandom optical lattice, *Science* **349**, 842 (2015).
- [36] H. P. Lüschen, P. Bordia, S. Scherg, F. Alet, E. Altman, U. Schneider, and I. Bloch, Observation of slow dynamics near the many-body localization transition in one-dimensional quasiperiodic systems, *Phys. Rev. Lett.* **119**, 260401 (2017).
- [37] H. P. Lüschen, S. Scherg, T. Kohlert, M. Schreiber, P. Bordia, X. Li, S. D. Sarma, and I. Bloch, Single-particle mobility edge in a one-dimensional quasiperiodic optical lattice, *Phys. Rev. Lett.* **120**, 160404 (2018).
- [38] J. Biddle, D. Priour Jr, B. Wang, and S. D. Sarma, Localization in one-dimensional lattices with non-nearest-neighbor hopping: Generalized anderson and aubry-andré models, *Phys. Rev. B* **83**, 075105 (2011).
- [39] J. Biddle and S. D. Sarma, Predicted mobility edges in one-dimensional incommensurate optical lattices: An exactly solvable model of anderson localization, *Phys. Rev. Lett.* **104**, 070601 (2010).
- [40] J. Biddle, B. Wang, D. Priour Jr, and S. D. Sarma, Localization in one-dimensional incommensurate lattices beyond the aubry-andré model, *Phys. Rev. A* **80**, 021603 (2009).
- [41] S. Ganeshan, J. Pixley, and S. D. Sarma, Nearest neighbor tight binding models with an exact mobility edge in one dimension, *Phys. Rev. Lett.* **114**, 146601 (2015).
- [42] D. Gelbwaser-Klimovsky and A. Aspuru-Guzik, On thermodynamic inconsistencies in several photosynthetic and solar cell models and how to fix them, *Chem. Sci.* **8**, 1008 (2017).
- [43] V. Gorini, A. Kossakowski, and E. C. G. Sudarshan, Completely positive dynamical semigroups of n-level systems, *J. Math. Phys.* **17**, 821 (1976).
- [44] G. Lindblad, On the generators of quantum dynamical semigroups, *Comm. Math. Phys.* **48**, 119 (1976).
- [45] H.-P. Breuer and F. Petruccione, *The theory of open quantum systems* (Oxford University Press, 2002).
- [46] For derivation of master equation in similar systems, see e.g. in the Appendix of P. H. Guimaraes, G. T. Landi, and M. J. de Oliveira, Nonequilibrium quantum chains under multisite lindblad baths, *Phys. Rev. E* **94**, 032139 (2016).
- [47] See Supplemental Material at [link by publisher] for detailed derivation of the master equation and more detailed analysis on the role of population spreading to the ENAQT mechanism.
- [48] L.-A. Wu and D. Segal, Energy flux operator, current conservation and the formal fourier's law, *J. Phys. A Math. Theor.* **42**, 025302 (2008).
- [49] X. Li, S. Ganeshan, J. Pixley, and S. D. Sarma, Many-body localization and quantum nonergodicity in a model with a single-particle mobility edge, *Phys. Rev. Lett.* **115**, 186601 (2015).
- [50] R. Modak and S. Mukerjee, Many-body localization in the presence of a single-particle mobility edge, *Phys. Rev. Lett.* **115**, 230401 (2015).
- [51] C. R. Harris, K. J. Millman, S. J. van der Walt, R. Gommers, P. Virtanen, D. Cournapeau, E. Wieser, J. Taylor, S. Berg, N. J. Smith, *et al.*, Array programming with numpy, *Nature* **585**, 357 (2020).
- [52] J. R. Johansson, P. D. Nation, and F. Nori, Qutip 2: A python framework for the dynamics of open quantum systems, *Comput. Phys. Commun.* **184**, 1234 (2013).
- [53] J. D. Hunter, Matplotlib: A 2d graphics environment, *Comput. Sci. Eng.* **9**, 90 (2007).

Supplemental Material: Environment-Assisted Quantum Transport in a One-Dimensional System with a Single-Particle Mobility Edge

Donny Dwiputra¹ and Freddy P. Zen^{1,2}

¹*Theoretical Physics Laboratory, Faculty of Mathematics and Natural Sciences,
Institut Teknologi Bandung, Jl. Ganesha 10, Bandung 40132, Indonesia*

²*Indonesian Center for Theoretical and Mathematical Physics (ICTMP), Bandung 40132, Indonesia*

I. DERIVATION OF THE MASTER EQUATION AND ITS STEADY STATE

For the microscopic derivation of the master equation, we use the Born-Markov and secular approximation to trace out the bath and write the Lindblad dissipator. This is most readily done using the eigenoperators method [45]. We first write the interaction Hamiltonians in eigenbasis η_k where $a_n = \sum_k S_{nk} \eta_k$ and S is the $N \times N$ unitary matrix obtained by diagonalizing H_S ,

$$H_{SB_1} = \sum_{l,\mu,k} g_\mu^{(1)} (S_{lk} \eta_k + S_{kl}^* \eta_k^\dagger) (\sigma_{\mu,l}^+ + \sigma_{\mu,l}^-), \quad (S1)$$

$$H_{SB_2} = \sum_{n,\mu,k,k'} g_\mu^{(2)} |S_{nk}|^2 \eta_k^\dagger \eta_{k'} (\sigma_{\mu,n}^+ + \sigma_{\mu,n}^-). \quad (S2)$$

In terms of the eigenoperators of H_S , we can write for each interaction $H_{SB_{(1,2)}} = \sum_{\omega,k} A_{i,k}(\omega) \otimes B_i$ where $i = \{l, n\}$ is the site index for SB_1 and SB_2 baths, respectively. Here the decomposed operator $A_{i,k}(\omega) \equiv \sum_{\epsilon' - \epsilon = \omega} \Pi(\epsilon) A_{i,k} \Pi(\epsilon')$ acts on the system, where $\Pi(\epsilon)$ is the projector onto eigenspace belonging to the eigenvalue ϵ of H_S , and B_i acts on the bath. The operator $A_{i,k}(\omega)$ is chosen to satisfy

$$[H, A_{i,k}(\omega)] = -\omega A_{i,k}(\omega). \quad (S3)$$

It follows that, for the respective baths, these eigenoperator will be

$$A_{l,k}(\omega) = S_{nk} \eta_k \delta_{\omega, +\epsilon_k} + S_{kn}^* \eta_k^\dagger \delta_{\omega, -\epsilon_k}, \quad (S4)$$

$$A_{n,k}(\omega) = S_{nk} S_{nk'} \eta_k^\dagger \eta_{k'} \delta_{\omega, \epsilon_{k'} - \epsilon_k}. \quad (S5)$$

while $B_i = \sum_\mu g_\mu^{(1,2)} (\sigma_{\mu,i}^+ + \sigma_{\mu,i}^-)$ for both $i = \{l, n\}$ [see Eq. (S1)]. Intuitively speaking, the coupling $(\eta_k + \eta_k^\dagger)$ and $\eta_k^\dagger \eta_k$ to the bath induces transitions in the system with the allowed energy ω .

For the each of above eigenoperators, the corresponding Lindblad dissipator is

$$\mathcal{D}[A_{i,k}] \rho = \sum_\omega \Gamma_i(\omega) \left[A_{i,k}(\omega) \rho A_{i,k}^\dagger(\omega) - \frac{1}{2} \{A_{i,k}^\dagger(\omega) A_{i,k}(\omega), \rho\} \right], \quad (S6)$$

where

$$\Gamma_i(\omega) = \int_0^\infty dt e^{i\omega t} \text{Tr}_B \left[(e^{iH_S t} B_i e^{-iH_S t}) B_i \frac{e^{-H_B/T_i}}{\text{Tr}(e^{-H_B/T_i})} \right] \quad (S7)$$

is the half sided Fourier transform of bath correlation functions. Thus, for SB_1 and SB_2 we get

$$\Gamma_i(\omega) = \begin{cases} J_i(\omega)[1 + n_i(\omega)], & \text{if } \omega > 0 \\ J_i(-\omega)n_i(-\omega), & \text{if } \omega < 0 \end{cases} \quad (S8)$$

where $n_i(\omega) = (e^{\beta_i \omega} + 1)^{-1}$ is the spin occupation number for SB_1 (SB_2) bath coupled to site l (n), and $J_i(\omega) = \sum_\mu \pi |g_\mu^{(1,2)}|^2 \delta(\omega - \epsilon_\mu)$ is the spectral density. for SB_2 , we denote the spectral density as $\gamma_n(\omega)$. Thus, by writing for $\omega > 0$ and $\omega < 0$ in a unified way, we can write the full dissipators as

$$\mathcal{D}_{SB_1} \rho = \sum_{l,k} |S_{lk}|^2 J(|\epsilon_k|) \left[(1 - n_l(\epsilon_k)) (\eta_k \rho \eta_k^\dagger - \frac{1}{2} \{ \eta_k^\dagger \eta_k, \rho \}) + n_l(\epsilon_k) (\eta_k^\dagger \rho \eta_k - \frac{1}{2} \{ \eta_k \eta_k^\dagger, \rho \}) \right], \quad (S9)$$

$$\begin{aligned} \mathcal{D}_{SB_2} \rho &= \sum_{n,k,k'} |S_{nk}|^2 |S_{nk'}|^2 \gamma_n(|\epsilon_{k'} - \epsilon_k|) \left[(1 - n_n(\epsilon_{k'} - \epsilon_k)) \theta(\epsilon_{k'} - \epsilon_k) + n_n(\epsilon_k - \epsilon_{k'}) \theta(\epsilon_k - \epsilon_{k'}) \right] \\ &\quad \times \left(\eta_k^\dagger \eta_{k'} \rho \eta_{k'}^\dagger \eta_k - \frac{1}{2} \{ \eta_k^\dagger \eta_{k'}, \rho \} \right), \end{aligned} \quad (S10)$$

where $\theta(\omega)$ is a step function. Following the main text, we assume that the dephasing bath is at $T = 0$ so that $n_n \rightarrow 0$. Hence, the second term in Eq. (S10) vanishes and, since we arrange the eigenvalues ϵ_k in increasing order, we can write the condition $k < k'$ for the summation indices. To simplify even further, we take the common $J_l = 1$ and $\gamma_n = \gamma$. Hence, the SB_2 dissipator is

$$\mathcal{D}_{SB_2}\rho = \sum_{n,k < k'} |S_{nk}|^2 |S_{nk'}|^2 \gamma \left(\eta_k^\dagger \eta_{k'} \rho \eta_{k'}^\dagger \eta_k - \frac{1}{2} \left\{ \eta_k^\dagger \eta_{k'}, \rho \right\} \right). \quad (\text{S11})$$

To find the NESS, we consider the corresponding adjoint master equation with $\mathcal{D}_{i,k}[A_{i,k}]^\dagger O = A_{i,k}^\dagger O A_{i,k} - 1/2\{A_{i,k}^\dagger A_{i,k}, O\}$ by replacing $O = \eta_k^\dagger \eta_{k'}$ and solving $\langle dO/dt \rangle = 0$. The solution can be found by using only the fundamental commutation relations which simplifies the adjoint dissipators considerably,

$$\mathcal{D}_{SB_1}^\dagger \left(\eta_k^\dagger \eta_{k'} \right) = \sum_l |S_{lk}|^2 \left(n_l(\epsilon_k) \delta_{kk'} - [1 - 2n_l(\epsilon_k)] \eta_k^\dagger \eta_{k'} \right), \quad (\text{S12})$$

$$\mathcal{D}_{SB_2}^\dagger \left(\eta_k^\dagger \eta_{k'} \right) = \frac{\gamma}{2} \sum_{i,n} (|S_{nk}|^2 + |S_{nk'}|^2) |S_{ni}|^2 \left(\eta_i^\dagger \eta_i \delta_{kk'} \theta(\epsilon_i - \epsilon_k) - \eta_k^\dagger \eta_{k'} \right). \quad (\text{S13})$$

It follows that the NESS density matrix element is

$$\langle \eta_k^\dagger \eta_{k'} \rangle = \delta_{kk'} \frac{\sum_l |S_{lk}|^2 n_l(\epsilon_k) + \gamma \sum_{i>k} \sum_n |S_{ni}|^2 |S_{nk}|^2 \langle \eta_i^\dagger \eta_i \rangle}{\sum_l |S_{lk}|^2 (1 - 2n_l(\epsilon_k)) + \gamma \sum_{i<k} \sum_n |S_{ni}|^2 |S_{nk}|^2}. \quad (\text{S14})$$

It is apparent that only the highest energy population, $\langle \eta_N^\dagger \eta_N \rangle$ is independent while lower energy populations should be solved via iterative backward calculation. Once the NESS is found, we can proceed to calculate the energy current with a similar calculation.

II. POPULATION SPREAD AND LOCALIZATION PROPERTIES OF THE STEADY STATE

In Fig. 2 of the main text we have studied the interplay between localization and population spread to ENAQT. Here we extend the discussion using by considering the average IPR $\langle I \rangle$ and the relative spread η/η_0 over all α 's and γ 's. The transitions of dephasing-independent f_{loc} in Fig. 2(b) of the main text, at $\alpha \approx 0.4$ (indicated by horizontal dotted lines) and less prominently at $\alpha \approx 0.9$, is nicely depicted here with the average IPR in the low dephasing regime until the quantum Zeno effect dominates the transport for $\gamma \gg 10^{-2}$.

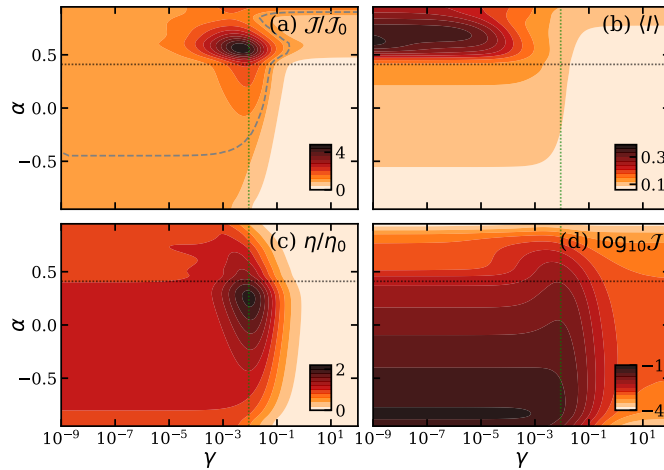


FIG. S1. Contour plots of (a) relative current $\mathcal{J}/\mathcal{J}_0$, (b) average IPR $\langle I \rangle$, (c) relative spread η/η_0 , and (d) current \mathcal{J} in logarithmic scale as a function of α and γ . Vertical lines indicate the value of γ where the relative spread is maximized and horizontal lines indicate α at which the average IPR (and also f_{loc}) undergo a transition. The parameters are the same as in Fig. 1 and 2 of the main text ($N = 22$, $\lambda = 0.4$, $T_h = 10^3$, $T_l = 10^{-1}$, and $\phi = \pi/3$).

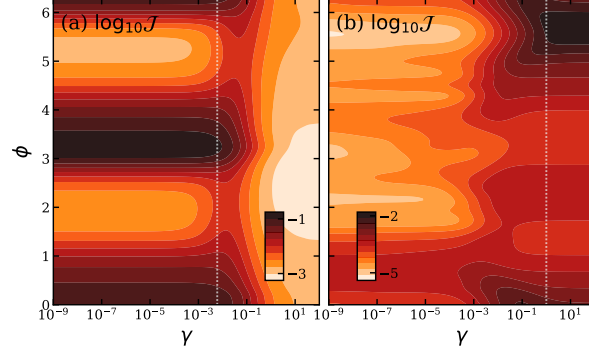


FIG. S2. Contour plots of current \mathcal{J} in logarithmic scale with $\lambda = 0.4$ and $\phi = \pi/3$ for (a) $\alpha = 0.1$ (delocalized regime; $f_{\text{loc}} = 0$) and (b) $\alpha = 0.9$ (localized regime; $f_{\text{loc}} \approx 0.5$). The vertical lines in (a) and (b) respectively correspond to current for the red ($\gamma = 0.06$) and blue ($\gamma = 1$) lines plotted in Fig. 3(a) of the main text.

The value of γ when the relative spread η/η_0 is maximized is indicated by the vertical dotted lines. By comparing Figs. S1(a) and S1(c), we can see that the maximum of η/η_0 for each α is in general coincides with the maximum ENAQT. To see this correlation more clearly, we can infer from the fact that in Fig. S1(d) the vertical dotted line crosses the inflection points of current \mathcal{J} which indicate the maximum enhancement for each constant α slice. We can simultaneously observe that η/η_0 is sensitive to the mobility edge as it captures the signature of $\langle I \rangle$ (and f_{loc}) transition at $\alpha \approx 0.4$ for the low γ regime.

Figures S2(a) and S2(b) show the current \mathcal{J} for delocalized and localized regimes, respectively. For clarity, we plot the current in logarithmic scale—in contrast to linear scale as in Fig. 3(a) of the main text. For the delocalized regime, current is maximized at low γ 's while for the localized regime it is at high γ 's. This contrasting behavior shows that the quantum Zeno effect may result in different consequences with the presence of mobility edges.

III. COMPARISON WITH THE OTHER MEASURE OF POPULATION SPREAD

This section clarify the reason of why we choose normalized entropy as the measure for population spread. In Fig. S3 we compare our measure η with the population spread Δ_n from Ref. [11], which is defined as

$$\Delta_n = 1 - \left(\frac{1}{N} \sum_i n_i - n_{\text{ext}} \right)^2 = 1 - \left(\frac{1}{N} - \sum_k |S_{Nk}|^2 p_k \right)^2, \quad (\text{S15})$$

where n_{ext} is the site basis population at the extraction site N . In energy basis it is $n_{\text{ext}} = \sum_k |S_{Nk}|^2 p_k$ where p_k is k -th energy population. Although Δ_n can mimic the \mathcal{J} (see Fig. S1(d)), its relative spread Δ_n/Δ_{n0} ($\Delta_{n0} \equiv \Delta_n(\gamma = 0)$) fails to contain the maximum and f_{loc} transition features of the relative current in Fig. S1(a) particularly for $\alpha > 0.4$ —which η/η_0 does so relatively well. Both features are crucial as they characterize the role of mobility edges in systems with ENAQT. In addition, the value η gives a broader variance while still bounded in $[0, 1]$.

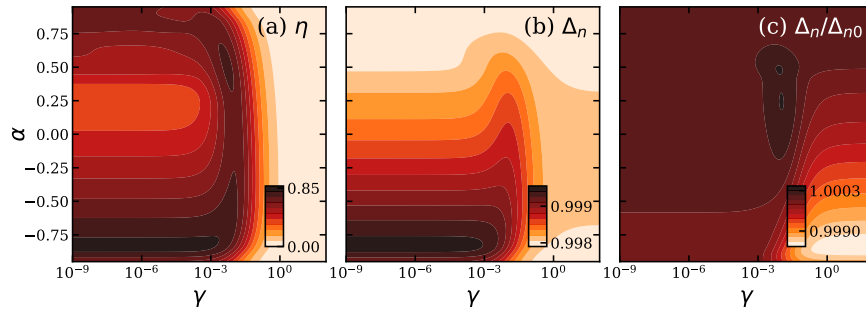


FIG. S3. Contour plots of (a) η , (b) Δ_n , and (c) its relative spread Δ_n/Δ_{n0} . The parameters are the same as in Fig. S1